

31 INTRODUCTION

32

33 Cell division orientation and timing must be carefully regulated in order to shape tissues and
34 determine cell fate, preventing defective embryonic development and diseases such as
35 cancer¹⁻³. Recent work has shown that mechanical cues from the extracellular environment
36 can influence cell division rate^{4,5} and orientation⁶⁻⁹. What remains unclear is whether dividing
37 cells are directly sensing mechanical forces or are responding to changes in cell shape
38 induced by these forces. This distinction is crucial as the molecular mechanisms involved in
39 either shape- or force-sensing could be very different^{10,11}.

40

41 Several mechanisms of division orientation control have been postulated in single cells, with
42 evidence for both shape- and stress-sensing^{7,12-14}. There is limited understanding of how
43 these models could apply to tissues, where cells are linked together by adhesions and it is far
44 more difficult to exclusively manipulate either cell shape or mechanical stress. Recent
45 evidence for a shape-sensing mechanism was found in the *Drosophila* pupal notum. The
46 spindle orientation protein, Mud (*Drosophila* orthologue of NuMA), localises at tricellular
47 junctions, recruiting force generators to orient astral microtubules in rounding mitotic cells¹⁵.
48 However, this mechanism has yet to be demonstrated in another system or related to
49 mechanical stress. In contrast, recent work in a stretched monolayer of MDCK cells has
50 indicated that division orientation may be mediated by a tension-sensing mechanism requiring
51 E-cadherin, although an additional role for cell shape sensing could not be excluded¹⁶.
52 Indeed, divisions in MDCK cells have also been found to align better with cell shape than a
53 global stretch axis, though local cell stress was not known in this case¹⁷.

54

55 Separating the roles of shape and stress in tissues will inevitably require an understanding of
56 how force is distributed through heterogeneous cell layers. Experimental methods of
57 assessing stress include laser ablation, atomic force microscopy and micro-aspiration^{9,18-20}.
58 Whilst informative, these techniques are invasive, perturbing the stress field through the
59 measurement, and usually require constitutive modelling for the measurement to be
60 interpreted^{21,22}. However, mathematical modelling combined with high quality fluorescence
61 imaging now provides the possibility of non-invasively inferring mechanical stress in tissues²³⁻
62 ²⁸.

63

64 In this article, we apply a reproducible strain to embryonic *Xenopus laevis* tissue to
65 investigate the roles of shape and stress in cell division in a multi-layered tissue. We
66 particularly focus on mathematically characterising local (cell-level) and global (tissue-level)
67 stress and the relation to cell shape and division. Our data suggest that mechanical stress is
68 not directly sensed for orienting the mitotic spindle, acting only to deform cell shape, but is
69 more actively read as a cue for mitosis.

70

71 **RESULTS**

72

73 **Application of tensile force to a multi-layered embryonic tissue**

74 To investigate the relationship between force, cell shape and cell division in a complex tissue,
75 we developed a novel system to apply reproducible mechanical strain to a multi-layered
76 embryonic tissue. Animal cap tissue was dissected from Stage 10 *Xenopus laevis* embryos
77 and cultured on a fibronectin-coated elastomeric PDMS substrate (Figure 1A). A uniaxial
78 stretch was applied to the PDMS substrate using an automated stretch device (Figure 1A),
79 and imaged using standard microscopy. The three-dimensional structure of the stretched
80 tissue (assessed using 3View EM) could be seen to comprise of approximately three cell
81 layers (Figure 1B), as would be expected in a stage 10 *Xenopus laevis* embryo^{29,30}, therefore
82 maintaining the multi-layered tissue structure present *in vivo*.

83

84 **Stretching elongates cell shape and reorients divisions.**

85 A 35% stretch of the PDMS substrate led to a $19.67 \pm 1.91\%$ (95% confidence interval)
86 elongation of apical cells in the animal cap along the stretch axis (measured change in length
87 of 1-dimensional lines drawn on opposite sides of the animal cap; displacement field shown in
88 Figure 1C). The difference in elongation between substrate and apical cells is presumably a
89 result of the mechanical stress being dissipated through multiple cell layers. The qualitative
90 change in cell shape was not as substantial as was previously observed in stretched
91 monolayers¹⁷ (Figure 1D).

92

93 We mathematically characterised shape using two parameters: orientation of the principal
94 axis of cell shape relative to the stretch axis (0°), θ_A , and cell circularity, C_A (derived in Section
95 1 of the Supplementary Document). C_A describes the degree of elongation of a cell (ranging
96 from 0 being a straight line to 1 being a perfect circle) and θ_A indicates the principal direction
97 in which this occurs. Stretching orients the majority of cells with the direction of stretch (Figure
98 1E) and causes a highly reproducible elongation of cell shape (Figure 1F). However, when
99 the substrate was held fixed following stretch, cell elongation reduced over time and returned
100 close to the unstretched shape profile after 90 minutes (95% confidence intervals of stretched
101 animal caps at $t = 90$ minutes overlap with unstretched caps; Figure 1F). Therefore, cells in
102 this tissue adapt to the elongation caused by stretching and do not behave like a purely
103 elastic material.

104

105 In unstretched tissue, division orientation, θ_D , was not significantly different from a uniform
106 distribution ($p = 0.36$, Kolmogorov-Smirnov test; Figure 1G). In contrast, divisions in the
107 stretched tissue were significantly oriented along the axis of stretch, ($p < 1.43 \times 10^{-9}$,
108 Kolmogorov-Smirnov test; Figure 1G), with 52% of divisions oriented within 30° of the stretch
109 axis (compared to 36% in unstretched).

110

111 **Shape-based models of division differ significantly depending on the cellular**
112 **characteristics used to define shape**

113 A shape-based 'long axis' division rule may explain why stretching reorients divisions.
114 However, the precise molecular mechanism behind shape-based models remains unclear
115 and may vary across cell type and tissue context^{7,9,13}. Past models have used different
116 characteristics to determine the shape of a cell, usually selecting one of the following: cell
117 area, cell perimeter and tricellular junction location. Though often used interchangeably, these
118 shape characteristics model different biological functions. We investigated their differences
119 and determined if one characteristic predicts division orientation better than the others.

120

121 We modelled cell shape by area, perimeter and tricellular junctions to derive three respective
122 measures of cell shape orientation, θ_A , θ_P , and θ_J , and circularity, C_A , C_P , and C_J
123 (Supplementary Document Section 1). Cells tend to have $C_P > C_A > C_J$ i.e. shape generally
124 appears less anisotropic using the perimeter-based measure. C_A and C_P (and
125 correspondingly θ_A and θ_P) are reasonably well correlated, while C_J (and θ_J) tends to coincide
126 less well with the others (Figure 2A&B). Thus a cell that appears round by area and perimeter
127 can have clear elongation as measured by tricellular junctions. This is intuitive for rounding
128 mitotic cells, where tricellular junctions can be distributed non-uniformly around the circular
129 periphery¹⁵. However, it is surprising that this can also be the case in cells with relatively
130 straight edges (Figure 2A''). Notably, cells in the *Xenopus* animal cap do not undergo the
131 dramatic mitotic cell rounding seen in some other systems¹⁵ (Supplemental Figure 1A&B).

132

133 **Tricellular junction placement is a better predictor of division orientation than cell area**
134 **or perimeter.**

135 Given that θ_A , θ_P , and θ_J are often highly correlated, division orientation is generally well
136 predicted by all three. We therefore focused on cases in which the orientations of shape
137 differed by at least 15°. In a pooled sample of 600 cells from stretched and unstretched
138 tissue, Only 7 cells were found to have $|\theta_A - \theta_P| \geq 15^\circ$. 58 satisfied $|\theta_A - \theta_J| \geq 15^\circ$ and 60
139 satisfied $|\theta_P - \theta_J| \geq 15^\circ$. In both cases, θ_J was a significantly better predictor of division angle
140 than random ($p < 0.0162$ when $|\theta_A - \theta_J| \geq 15^\circ$; $p < 0.0042$ when $|\theta_P - \theta_J| \geq 15^\circ$; Mann-
141 Whitney U test), but θ_A and θ_P were not (Figure 2C&D). Furthermore, C_A , C_P , and C_J were all
142 significantly higher in these subpopulations (Supplemental Figure 1C&D; 95% confidence
143 intervals do not overlap), indicating that these cells are rounder, yet can still effectively orient
144 their spindle in-line with their tricellular junctions. This result is strengthened considering that
145 tricellular junctions provide fewer data points than area or perimeter, thus junctional data may
146 more susceptible to geometric error than area and perimeter.

147

148 In unstretched tissue, cells which we classed as "rounded" ($C_A > 0.65$; Figure 2E) showed no
149 significant correlation between θ_A and θ_D or θ_P and θ_D , as could be expected from previous
150 work⁷. However, θ_J was significantly aligned with division angle in these round cells, when

151 compared to random ($p = 0.025$, Mann-Whitney U test) (Figure 2F&G). This degree of
152 sensitivity is striking and further demonstrates that tricellular junction-sensing could function
153 effectively in round cells, which may have previously been thought to divide at random.

154

155 **Local cell shape aligns with local stress and predicts division orientation better than** 156 **global stretch and stress**

157 Contrary to observations in monolayers¹⁶, we found that cells in stretched tissue divide
158 according to cell shape both when θ_J is oriented with (Figure 3A) and against (Figure 3B&C)
159 the direction of stretch. These data indicate that global stretch direction is a poor predictor of
160 division angle when compared to cell shape. However, little is known about the local stress
161 distribution around cells subjected to a stretch, which may not coincide with global stress in
162 such a geometrically heterogeneous material.

163

164 We extended a popular vertex-based model to mathematically characterise cell stress^{24-26,28}.
165 Predicted orientations of forces from the model have been found to be in accordance with
166 laser ablation experiments^{31,32}, indicating that the model can provide a physically relevant
167 description of cellular stresses. Our methodology allows relative cell stress to be inferred
168 solely from the positions of cell vertices, without invasively altering the mechanical
169 environment (Supplementary Document, Section 2). The model predicts that the orientation of
170 cell shape based on tricellular junctions, θ_J , aligns exactly with the principal axis of local
171 stress²⁸ (Figure 3D). We demonstrated this computationally in stretched tissue by simulating a
172 uniaxial stretch (Figure 3E-F). Following stretch, we see that local cell stress remains aligned
173 with θ_J , rather than the global stress along the x-axis. Much previous work assumes that the
174 local axis of stress coincides with the global stress. Significantly, the model predicts that a
175 stress-sensing mechanism would align divisions in the same direction as a shape-based
176 mechanism (as in Figure 3B).

177

178 **The magnitude of cell stress does not correlate with the alignment of division angle** 179 **and tricellular junction positioning**

180 If a stress-sensing mechanism were contributing to orienting division, we hypothesised that
181 cells under higher net tension or compression might orient division more accurately with the
182 principal axis of stress (θ_J). We infer relative tension/compression using the isotropic
183 component of stress, effective pressure (P^{eff})²⁸:

$$P^{\text{eff}} = \frac{\tilde{A}}{\tilde{A}_0} - 1 + \frac{\Gamma \tilde{L}^2}{2\tilde{A}} + \frac{\Lambda \tilde{L} \sqrt{\tilde{A}_0}}{4\tilde{A}}$$

184 where \tilde{A} is cell area, \tilde{L} is perimeter, \tilde{A}_0 is the preferred area and (Λ, Γ) are model parameters,
185 defined in Section 2 of the Supplementary Document and inferred from data²⁸. Cells under
186 net tension have $P^{\text{eff}} > 0$, whereas $P^{\text{eff}} < 0$ indicates net compression. We provide a novel
187 method for estimating \tilde{A}_0 in Section 3 of the Supplementary Document. A representative

188 segmentation, showing cells predicted to be under net tension and compression, from an
189 unstretched experiment is given in Figure 3G. Interestingly, we found no correlation between
190 the value of P^{eff} (relative isotropic stress) and the alignment of division orientation to θ_J
191 ($|\theta_D - \theta_J|$) (Supplemental Figure 2A). Accordingly, we found that knockdown of the tension
192 sensor, vinculin, in stretched tissue does not affect division orientation relative to θ_J
193 (Supplemental Figure 2C).

194 The mechanical state of a cell may also be characterised by shear stress, ξ (defined as the
195 eigenvalue of the deviatoric component of the stress tensor, see Section 2 of the
196 Supplementary Document). Larger values of $|\xi|$ indicate increased cellular shear stress.
197 Again, we found no correlation between ξ and the alignment of division to θ_J (Supplemental
198 Figure 2B).

199

200 Despite the lack of correlation with stress magnitude, cell shape anisotropy, measured by C_J ,
201 correlates significantly with $|\theta_D - \theta_J|$ ($p < 3.04 \times 10^{-10}$, Spearman rank correlation coefficient;
202 Figure 3H), with elongated cells having θ_D aligned with θ_J significantly better than round cells
203 ($p < 1.64 \times 10^{-8}$; Figure 3I).

204

205 **Cadherin is required for positioning the mitotic spindle relative to cell shape**

206 Immunofluorescence staining of β -catenin confirmed that adherens junctions were distributed
207 along the apical cell cortex, but particularly concentrated at the meeting points of three or
208 more cells (Supplemental Figure 3A). To test a functional requirement for adherens junctions
209 in orienting the spindle, we focused on maternal C-cadherin (cadherin 3), which is expressed
210 at the highest level in Stage 10-11 *Xenopus* embryos^{33,34}. We used two constructs to
211 manipulate C-cadherin in the tissue: C-cadherin FL -6xmyc (CdhFL: Full length C-cadherin
212 with 6xmyc tags at the intracellular c-terminus) and C-cadherin ΔC -6xmyc (Cdh ΔC : C-
213 cadherin with extracellular and transmembrane domains, but lacking the cytosolic domain)
214 (Figure 4A)³⁵. CdhFL- and Cdh ΔC -injected embryos developed normally up to Stage 10/11
215 (Figure 4B), but the majority of embryos failed to complete gastrulation³³ (and data not
216 shown). We observed no change in the cumulative distribution of cell circularities in CdhFL-
217 and Cdh ΔC -injected tissues compared to control tissue (Supplemental Figure 3B). We also
218 saw no difference in the rate of cell divisions (data not shown).

219

220 Cdh ΔC -injected tissue was elongated by application of stretch (Figure 4C), but showed worse
221 alignment of divisions to stretch direction compared to uninjected control and CdhFL-injected
222 tissue (Figure 4D; Mann-Whitney U test $p < 0.0162$ for Cdh ΔC less than CdhFL). Moreover,
223 unstretched Cdh ΔC -injected tissue showed a significant decrease in the alignment of division
224 angle to θ_J , when compared to uninjected controls (Figure 4E; $p < 0.016$ Kolmogorov-Smirnov
225 test on distributions differing), though both were significantly different to random (control: $p <$
226 3.6×10^{-11} ; Cdh ΔC : $p < 4.3 \times 10^{-11}$; Kolmogorov Smirnov test). We overexpressed C-cadherin in

227 the cell cortex by injecting CdhFL, which led to an increased localisation of the adherens
228 junction component, β -catenin, around the entire cell perimeter (Supplemental Figure 3A).
229 Focussing on cells which satisfied $|\theta_P - \theta_J| \geq 15^\circ$, we found the striking result that division
230 orientation was now significantly well predicted by cell perimeter, but no longer by tricellular
231 junctions (Figure 4F; $p < 0.0027$ for alignment θ_D to θ_P , but not significant for θ_D to θ_J ; Mann-
232 Whitney U test). Therefore, overexpression of CdhFL was sufficient to switch division
233 orientation from alignment with tricellular junctions to alignment with the shape of the entire
234 cortex.

235

236 **Cell division rate is temporarily increased following change in global stress**

237 Stretch elicited a reproducible and significant increase in cell division rate, with 6.47 ± 1.12 %
238 of cells dividing per hour in the stretched tissue compared to 3.22 ± 0.55 % in unstretched
239 tissue (Figure 5A, 95% confidence intervals do not overlap), as reported for cultured cells and
240 monolayers^{13,17,36}. We roughly classify two distinct periods of division after stretch; there is an
241 initial period of high proliferation (8.1% cells undergoing division per hour; Figure 5B), which
242 drops, after 40-60 minutes, to near-unstretched control levels (4.2% cells undergoing division
243 per hour). Stretching increases apical tissue area by $6 \pm 2.69\%$ (95% confidence interval),
244 and is predicted to increase global stress by increasing individual values of P^{eff} . We sought to
245 determine whether the increase in division rate is a response to these changes.

246

247 In both stretched and unstretched experiments, dividing cells had a larger area than the
248 population, being about 22.7% and 25.7% larger on average respectively (Figure 5C).
249 Similarly, the mean perimeter was significantly larger in the dividing cells by about 14.1% in
250 unstretched and 13.8% in stretched (Figure 5D). However, there was no significant difference
251 in the level of cell elongation in dividing cells (Supplemental Figure 2D). Crucially, we found
252 that dividing cells were more likely to be under predicted net tension than compression
253 (Figure 5E, more cells in red region). However, P^{eff} is correlated with cell area (though the
254 two are not always equivalent), thus a further perturbation was required to separate their
255 effects.

256

257 **Loss of myosin II reduces cell contractility**

258 We perturbed the mechanical properties of the tissue with targeted knockdown of non-muscle
259 myosin II using a previously published morpholino³⁷. As expected, myosin II knockdown
260 disrupted cytokinesis, seen by the formation of 'butterfly' shaped nuclei, where daughter cells
261 had not fully separated (Figure 6A&B). However, division rate and orientation could still be
262 assessed using the same methods described for control tissue. Myosin II is known to
263 generate contractility within a tissue³⁸⁻⁴⁰. Accordingly, we found evidence for reduced
264 contractility in the myosin II MO tissue by observing that cells were much slower at adapting
265 to stretch, remaining elongated for longer (compare Figure 6C to Figure 1F).

266

267 **Myosin II is required for mitotic entry in unstretched tissue**

268 Somewhat surprisingly, considering suggestions that myosin II may play a stress-sensing role
269 in orienting the spindle⁹, we found that alignment of division angle to stretch and θ_j was
270 unaffected in myosin II knockdown experiments (Figure 6D&E). In contrast, proliferation rate
271 was significantly affected, with divisions virtually ceasing in unstretched myosin II MO tissue.
272 Strikingly, stretching the myosin II MO tissue increased the division rate to significantly higher
273 levels (Figure 6F). Thus myosin II is required to cue cells into division in the unstretched
274 tissue, but this can be partially overridden by applying an external loading. Unlike in control
275 experiments, dividing cells in myosin II knockdown stretch experiments were not significantly
276 larger than the population in area (Figure 6G) or perimeter (Figure 6H). This suggests that cell
277 area has been uncoupled as a cue to divide in the myosin II knockdowns.

278

279 **DISCUSSION**

280

281 Previous models of cell division have demonstrated that specific features of cell shape, such
282 as the cell cortex or tricellular junctions, may be important in orienting the spindle^{7,15,41,42}. We
283 have presented a framework for characterising cell shape in terms of its area, perimeter or
284 tricellular junctions (Supplementary Document). We find that the principal axis of shape
285 defined by tricellular junctions is the best predictor of division angle and aligns exactly with the
286 principal axis of local stress. However, division angle is not better predicted in cells with
287 higher/lower relative isotropic or shear stress and is unaffected by knockdown of vinculin in
288 stretched tissue. This finding shares similarities with observations in the *Drosophila* pupal
289 notum, where tricellular junctions have been hypothesised to localise force generators¹⁵.
290 Notably, however, *Xenopus* animal cap cells do not undergo the dramatic mitotic rounding
291 exhibited by cells in the notum.

292

293 Cell-cell adhesion has been linked to spindle orientation in MDCK cells, where E-cadherin
294 instructs LGN/NuMA assembly at cell-cell contacts to orient divisions⁴³. E-cadherin polarises
295 along a stretch axis, reorienting divisions along this axis rather than according to cell shape¹⁶.
296 In accordance, we find division is less well predicted by shape in embryos injected with C-
297 cadherin ΔC -6xmyc, lacking the cytosolic domain. Interestingly, over-expression of C-
298 cadherin around the entire cell cortex leads to division being best predicted by a perimeter-
299 based shape axis. As β -catenin is increased around the cell cortex, this may be due to
300 recruitment of spindle orientation proteins, such as NuMA/LGN⁴³. We, and others, find that
301 cadherin is most highly localised at the meeting points between three or more cells in wild-
302 type *Xenopus* epithelium³⁵. We suggest that these “hotspots” of cadherin localisation recruit
303 spindle orientation machinery such as LGN/NuMA, reminiscent of the Mud-dependent
304 tricellular junction-sensing mechanism in the *Drosophila* pupal notum¹⁵.

305

306 Stretching increases proliferation rate, which correlates with cell area, perimeter and effective
307 pressure. We see almost no proliferation in unstretched myosin II MO experiments, although,
308 rather strikingly, the division rate is significantly increased following stretch. Dividing myosin II
309 MO cells are not significantly larger in area or perimeter than the population as a whole,
310 indicating that cell area has been decoupled as a division cue. Considering the established
311 role of myosin II as a force generator^{39,40,44}, it is possible that the myosin II MO cells cannot
312 generate enough internal contractility in neighbouring cells to engage the mechanical cues
313 required for mitotic entry. Myosin II has also been shown to function in stress-sensing
314 pathways^{45,46}, which may explain why the proliferation rate in stretched myosin II MO cells
315 does not reach the levels of stretched controls. Contrary to findings in other systems⁹, loss of
316 myosin II does not alter division orientation relative to cell shape.

317

318 In conclusion, we have combined whole-tissue stretching with a biomechanical model to
319 propose separate roles for cell shape and mechanical stress in orienting the spindle and
320 cueing mitosis (summarised in Figure 7). The mechanism involved in orienting the mitotic
321 spindle does not appear to sense relative cell stress directly. Instead, division is best
322 predicted by an axis of shape defined by tricellular junctions and is dependent on functional
323 cadherin. In contrast to this shape-based mechanism, we find that cells may directly sense
324 mechanical stress as a cue for mitotic entry, in a myosin II-dependent manner.

325

326 **Materials and Methods**

327

328 ***Xenopus laevis* embryos and microinjection**

329 *Xenopus laevis* embryos were obtained and injected as described previously⁴⁷. RNA was
330 synthesised as described previously⁴⁸ and microinjected at the following needle
331 concentrations: 0.5 mg/ml GFP- α -tubulin; 0.1 mg/ml cherry-histone2B⁴⁹; 0.125 mg/ml
332 cadherin 3a full length:6x myc-tag; 0.125 mg/ml cadherin 3a deleted cytosolic domain:6x myc-
333 tag³⁵. Morpholinos prepared as 1mM stocks (diluted in water) were heated at 65°C for 5
334 minutes and microinjected at a needle concentration of 1mM and needle volume of 2.5nl into
335 all cells of four-cell stage embryos. The morpholinos used were MHC-B (Myosin Heavy
336 Chain-B, myosin II) MO (5'-CTTCCTGCCCTGGTCTCTGTGACAT-3';³⁷), Vinculin MO (5'-
337 TATGGAAGACCGGCATCTTGGCAAT-3');⁵⁰) and standard control MO (5'-
338 CCTCTTACCTCAGTTACAATTTATA-3'; Gene Tools LLC). All embryos were incubated at
339 16°C for approximately 20 hours prior to animal cap dissection.

340

341 **Animal cap dissection and culture**

342 Animal cap tissue was dissected from the embryo at stage 10 of development (early gastrula
343 stage) following a previously described protocol⁵¹, and cultured in Danilchik's for Amy explant
344 culture media (DFA; 53mM NaCl₂, 5mM Na₂CO₃, 4.5mM Potassium gluconate, 32mM
345 Sodium gluconate, 1mM CaCl₂, 1mM MgSO₄) on a 20mm × 20mm elastomeric PDMS

346 (Sylgard 184, SLS) membrane made in a custom mold and coated with fibronectin (fibronectin
347 from bovine plasma, Sigma). Explants were held in place by a coverslip fragment. Each
348 membrane was then incubated at 18°C for at least 2 hours prior to imaging.

349

350 **Animal cap stretch manipulation and confocal imaging**

351 Each PDMS membrane was attached to a stretch apparatus (custom made by Deben UK
352 Limited) fixed securely to the stage of a Leica TCS SP5 AOBS upright confocal and a 0.5mm
353 (to remove sag on the membrane) or 8.6mm uniaxial stretch was applied for unstretched and
354 stretched samples respectively.

355

356 Images were collected on a Leica TCS SP5 AOBS upright confocal using a 20x/0.50 HCX
357 Apo U-V-I (W (Dipping Lens)) objective and 2x confocal zoom. The distance between optical
358 sections was maintained at 4.99µm and the time interval between each frame was 20
359 seconds, with each samples being imaged for up to 2.5 hours. Maximum intensity projections
360 of these 3D stacks are shown in the results.

361

362 **Image analysis**

363 Image analysis was performed using ImageJ⁵². Cell division orientation was quantified using
364 the straight-line tool to draw a line between the dividing nuclei of a cell in late anaphase (a
365 stage in mitosis where division orientation is set and the spindle undergoes no further rotation
366 ^{47,53}). Using the ROI manager the angle of division relative to stretch (horizontal axis) was
367 recorded along with the frame and location of the division. Single cell edges and junctions
368 were manually traced 40s before NEB using the freehand paintbrush tool. The whole
369 population of cells in the apical layer of the animal cap was manually traced, along with
370 peripheral junctions and cell centres, using the freehand paintbrush tool. Segmentation of the
371 cell boundaries was performed using in-house Python scripts implementing a watershed
372 algorithm. Geometric features of the cells, such as area and perimeter, were extracted and
373 analysed in Python. For further details on how cell shape was characterised using the
374 segmented images, please see the Supplementary Document.

375

376 **Data analysis**

377 The data analysis and plotting was carried out using in-house Python scripts. Statistical tests
378 were performed using the SciPy library⁵⁴. Mann-Whitney U tests were used to assess if rose
379 histograms were distributed closer to zero. Kolmogorov-Smirnov tests were used to assess if
380 two distributions were significantly different. Otherwise, bootstrapping with 95% confidence
381 intervals, which allow the precision of the estimate to be seen⁵⁵, were used to assess
382 significance.

383

384 **Immunofluorescence**

385 Embryos were fixed at stage 12 following the protocol previously detailed by Jones et al.,
386 (2014)⁵⁶. Embryos were incubated in primary and secondary antibodies in TBSN/BSA (Tris-
387 buffered saline: 155mM NaCl, 10mM Tris-Cl [pH 7.4]; 0.1% Nonidet P-40; 10 mg/ml BSA)
388 overnight at 4°C, with five 1 hour washes with TBSN/BSA following each incubation. Primary
389 antibodies were: anti- β -catenin at 1:200 dilution, raised in rabbit (Abcam) and anti c-myc
390 9E10 at 1:1000 dilution, raised in mouse (Santa-cruz). Alexa Fluor secondary antibodies, anti-
391 rabbit 488 and anti-mouse 568 (Invitrogen) were used at a dilution of 1:400. After staining,
392 embryos were methanol dehydrated, then cleared and mounted in Murray's Clear (2:1, benzyl
393 benzoate:benzyl alcohol; ⁵⁷).

394 Images were collected on a Leica TCS SP5 AOBS inverted confocal using a 63x HCX PL
395 APO (Oil λ BL) objective and 1024 x 1024 format. Single confocal slices are shown in the
396 results.

397

398 **Implementation of the vertex-based model**

399 The numerical simulations of the vertex-based model were carried out using the same scripts
400 outlined in section 3.8 of ²⁸. Model parameters used for all simulations were $(A, I) =$
401 $(-0.259, 0.172)$, determined using a fitting procedure described in ²⁸.

402

403 **Acknowledgements**

404 ANB was supported by a BBSRC studentship. SW, GSV and GG were supported by a
405 Wellcome Trust/Royal Society Sir Henry Dale Fellowship to SW [098390/Z/12/Z] with
406 additional funding from the Wellcome Trust ISSF [105610/Z/14/Z]. The Bioimaging Facility
407 microscopes used in this study were purchased with grants from BBSRC, Wellcome and the
408 University of Manchester Strategic Fund. Thanks to Peter March and Roger Meadows for
409 their help with the microscopy and to Lance Davidson for sharing Cadherin constructs. Also,
410 special thanks to Viki Allan, Tom Millard and Nancy Papalopulu for their critical reading of the
411 manuscript.

412

413 **Bibliography**

414

415

416

- 417 1. Quyn, A. J. *et al.* Spindle Orientation Bias in Gut Epithelial Stem Cell Compartments Is
418 Lost in Precancerous Tissue. *Cell Stem Cell* **6**, 175–181 (2010).
- 419 2. Pease, J. C. & Tirnauer, J. S. Mitotic spindle misorientation in cancer – out of
420 alignment and into the fire. *J Cell Sci* **124**, 1007–1016 (2011).
- 421 3. Mishra, P. & Chan, D. C. Mitochondrial dynamics and inheritance during cell division,
422 development and disease. *Nature Reviews Molecular Cell Biology* **15**, 634–646
423 (2014).
- 424 4. Streichan, S. J., Hoerner, C. R., Schneidt, T., Holzer, D. & Hufnagel, L. Spatial
425 constraints control cell proliferation in tissues. *PNAS* **111**, 5586–5591 (2014).
- 426 5. Benham-Pyle, B. W., Pruitt, B. L. & Nelson, W. J. Mechanical strain induces E-
427 cadherin-dependent Yap1 and beta-catenin activation to drive cell cycle entry. *Science*
428 **348**, 1024–1027 (2015).
- 429 6. Mao, Y. *et al.* Planar polarization of the atypical myosin Dachs orients cell divisions in

- 430 *Drosophila*. *Genes Dev.* **25**, 131–136 (2011).
- 431 7. Minc, N., Burgess, D. & Chang, F. Influence of cell geometry on division-plane
432 positioning. *Cell* **144**, 414–426 (2011).
- 433 8. Legoff, L., Rouault, H. & Lecuit, T. A global pattern of mechanical stress polarizes cell
434 divisions and cell shape in the growing *Drosophila* wing disc. *Development* **140**, 4051–
435 4059 (2013).
- 436 9. Campinho, P. *et al.* Tension-oriented cell divisions limit anisotropic tissue tension in
437 epithelial spreading during zebrafish epiboly. *Nature cell biology* **15**, 1405–1414
438 (2013).
- 439 10. Nestor-Bergmann, A., Goddard, G. & Woolner, S. Force and the spindle: Mechanical
440 cues in mitotic spindle orientation. *Semin. Cell Dev. Biol.* **34**, 133–139 (2014).
- 441 11. Luo, T., Mohan, K., Iglesias, P. A. & Robinson, D. N. Molecular mechanisms of cellular
442 mechanosensing. *Nature Materials* **12**, 1063–1070 (2013).
- 443 12. Minc, N. & Piel, M. Predicting division plane position and orientation. *Trends in Cell*
444 *Biology* **22**, 193–200 (2012).
- 445 13. Fink, J. *et al.* External Forces Control Mitotic Spindle Positioning. *Nature cell biology*
446 **13**, 771–778 (2011).
- 447 14. Théry, M., Pépin, A., Dressaire, E., Chen, Y. & Bornens, M. Cell distribution of stress
448 fibres in response to the geometry of the adhesive environment. *Cell Motility and the*
449 *Cytoskeleton* **63**, 341–355 (2006).
- 450 15. Bosveld, F. *et al.* Epithelial tricellular junctions act as interphase cell shape sensors to
451 orient mitosis. *Nature* **530**, 495–+ (2016).
- 452 16. Hart, K. C. *et al.* E-cadherin and LGN align epithelial cell divisions with tissue tension
453 independently of cell shape. *Proc. Natl. Acad. Sci. U.S.A.* **114**, E5845–E5853 (2017).
- 454 17. Wyatt, T. P. J. *et al.* Emergence of homeostatic epithelial packing and stress
455 dissipation through divisions oriented along the long cell axis. *PNAS* **112**, 5726–5731
456 (2015).
- 457 18. Hutson, M. S. *et al.* Forces for morphogenesis investigated with laser microsurgery
458 and quantitative modeling. *Science* **300**, 145–149 (2003).
- 459 19. Hoh, J. H. & Schoenenberger, C. A. Surface morphology and mechanical properties of
460 MDCK monolayers by atomic force microscopy. *J Cell Sci* **107 (Pt 5)**, 1105–1114
461 (1994).
- 462 20. Davidson, L., Dassow, von, M. & Zhou, J. Multi-scale mechanics from molecules to
463 morphogenesis. *Int. J. Biochem. Cell Biol.* **41**, 2147–2162 (2009).
- 464 21. Stooke-Vaughan, G. A., Davidson, L. A. & Woolner, S. *Xenopus* as a model for
465 studies in mechanical stress and cell division. *Genesis* **55**, e23004 (2017).
- 466 22. Sugimura, K., Lenne, P.-F. & Graner, F. Measuring forces and stresses in situ in living
467 tissues. *Development* **143**, 186–196 (2016).
- 468 23. Xu, G.-K., Liu, Y. & Li, B. How do changes at the cell level affect the mechanical
469 properties of epithelial monolayers? *Soft Matter* **11**, 8782–8788 (2015).
- 470 24. Brodland, G. W. *et al.* CellFIT: A Cellular Force-Inference Toolkit Using Curvilinear
471 Cell Boundaries. *PLoS ONE* **9**, e99116 (2014).
- 472 25. Ishihara, S. & Sugimura, K. Bayesian inference of force dynamics during
473 morphogenesis. *J. Theoret. Biol.* **313**, 201–211 (2012).
- 474 26. Chiou, K. K., Hufnagel, L. & Shraiman, B. I. Mechanical stress inference for two
475 dimensional cell arrays. *PLoS Comput. Biol.* **8**, e1002512 (2012).
- 476 27. Feroze, R., Shawky, J. H., Dassow, von, M. & Davidson, L. A. Mechanics of
477 blastopore closure during amphibian gastrulation. *Dev. Biol.* **398**, 57–67 (2015).
- 478 28. Nestor-Bergmann, A., Goddard, G., Woolner, S. & Jensen, O. Relating cell shape and
479 mechanical stress in a spatially disordered epithelium using a vertex-based model.
480 *Math. Med. Biol.* (2017). doi:10.1093/imammb/dqx008
- 481 29. Keller, R. E. & Schoenwolf, G. C. An SEM study of cellular morphology, contact, and
482 arrangement, as related to gastrulation in *Xenopus laevis*. *Development Genes and*
483 *Evolution* (1977).
- 484 30. Keller, R. E. The cellular basis of epiboly: an SEM study of deep-cell rearrangement
485 during gastrulation in *Xenopus laevis*. *J Embryol Exp Morphol* **60**, 201–234 (1980).
- 486 31. Farhadifar, R., Röper, J. C., Aigouy, B., Eaton, S. & Jülicher, F. The influence of cell
487 mechanics, cell-cell interactions, and proliferation on epithelial packing. *Current*
488 *Biology* **17**, 2095–2104 (2007).
- 489 32. Landsberg, K. P. *et al.* Increased Cell Bond Tension Governs Cell Sorting at the

- 490 Drosophila Anteroposterior Compartment Boundary. *Current Biology* **19**, 1950–1955
491 (2009).
- 492 33. Lee, C. H. & Gumbiner, B. M. Disruption of Gastrulation Movements in *Xenopus* by a
493 Dominant-Negative Mutant for C-Cadherin. *Dev. Biol.* **171**, 363–373 (1995).
- 494 34. Heasman, J. *et al.* A Functional Test for Maternally Inherited Cadherin in *Xenopus*
495 Shows Its Importance in Cell-Adhesion at the Blastula Stage. *Development* **120**, 49–
496 57 (1994).
- 497 35. Kurth, T. *et al.* Immunocytochemical studies of the interactions of cadherins and
498 catenins in the early *Xenopus* embryo. *Dev. Dyn.* **215**, 155–169 (1999).
- 499 36. Streichan, S. J., Hoerner, C. R., Schneidt, T., Holzer, D. & Hufnagel, L. Spatial
500 constraints control cell proliferation in tissues. *PNAS* **111**, 5586–5591 (2014).
- 501 37. Skoglund, P., Rolo, A., Chen, X., Gumbiner, B. M. & Keller, R. Convergence and
502 extension at gastrulation require a myosin IIB-dependent cortical actin network.
503 *Development* **135**, 2435–2444 (2008).
- 504 38. Effler, J. C. *et al.* Mitosis-Specific Mechanosensing and Contractile-Protein
505 Redistribution Control Cell Shape. *Current Biology* **16**, 1962–1967 (2006).
- 506 39. Clark, A. G., Wartlick, O., Salbreux, G. & Paluch, E. K. Stresses at the Cell Surface
507 during Animal Cell Morphogenesis. *Current Biology* **24**, R484–R494 (2014).
- 508 40. Gutzman, J. H., Sahu, S. U. & Kwas, C. Non-muscle myosin IIA and IIB differentially
509 regulate cell shape changes during zebrafish brain morphogenesis. *Dev. Biol.* **397**,
510 103–115 (2015).
- 511 41. Luxenburg, C., Pasolli, H. A., Williams, S. E. & Fuchs, E. Developmental roles for Srf,
512 cortical cytoskeleton and cell shape in epidermal spindle orientation. *Nature cell*
513 *biology* **13**, 203–U51 (2011).
- 514 42. Hertwig, O. Ueber den Werth der ersten Furchungszellen für die Organbildung des
515 Embryo Experimentelle Studien am Frosch-und Tritonei. *Archiv f. mikrosk. Anat.* **42**,
516 662–807 (1893).
- 517 43. Gloerich, M., Bianchini, J. M., Siemers, K. A., Cohen, D. J. & Nelson, W. J. Cell
518 division orientation is coupled to cell-cell adhesion by the E-cadherin/LGN complex.
519 *Nat Commun* **8**, (2017).
- 520 44. Vicente-Manzanares, M., Ma, X., Adelstein, R. S. & Horwitz, A. R. Non-muscle myosin
521 II takes centre stage in cell adhesion and migration. *Nature Reviews Molecular Cell*
522 *Biology* **10**, 778–790 (2009).
- 523 45. Hirata, H. *et al.* Actomyosin bundles serve as a tension sensor and a platform for ERK
524 activation. *EMBO Rep.* **16**, 250–257 (2015).
- 525 46. Priya, R. *et al.* Feedback regulation through myosin II confers robustness on RhoA
526 signalling at E-cadherin junctions. *Nature cell biology* **17**, 1282–1293 (2015).
- 527 47. Woolner, S. & Papalopulu, N. Spindle Position in Symmetric Cell Divisions during
528 Epiboly Is Controlled by Opposing and Dynamic Apicobasal Forces. *Developmental*
529 *cell* **22**, 775–787 (2012).
- 530 48. Sokac, A. M., Co, C., Taunton, J. & Bement, W. Cdc42-dependent actin
531 polymerization during compensatory endocytosis in *Xenopus* eggs. *Nature cell biology*
532 **5**, 727–732 (2003).
- 533 49. Kanda, T., Sullivan, K. F. & Wahl, G. M. Histone-GFP fusion protein enables sensitive
534 analysis of chromosome dynamics in living mammalian cells. *Current Biology* **8**, 377–
535 385 (1998).
- 536 50. Petridou, N. I., Stylianou, P. & Skourides, P. A. A dominant-negative provides new
537 insights into FAK regulation and function in early embryonic morphogenesis.
538 *Development* **140**, 4266–4276 (2013).
- 539 51. Joshi, S. D. & Davidson, L. A. Live-cell imaging and quantitative analysis of embryonic
540 epithelial cells in *Xenopus laevis*. *J Vis Exp* (2010). doi:10.3791/1949
- 541 52. Schneider, C. A., Rasband, W. S. & Eliceiri, K. W. NIH Image to ImageJ: 25 years of
542 image analysis. *Nat. Methods* **9**, 671–675 (2012).
- 543 53. Woolner, S., O'Brien, L. L., Wiese, C. & Bement, W. M. Myosin-10 and actin filaments
544 are essential for mitotic spindle function. *J Cell Biol* **182**, 77–88 (2008).
- 545 54. Jones, E. & Oliphant, P. SciPy: Open Source Scientific Tools for Python. (2001).
546 Available at: <http://www.scipy.org/>. (Accessed: 8 June 2017)
- 547 55. Nakagawa, S. & Cuthill, I. C. Effect size, confidence interval and statistical
548 significance: a practical guide for biologists. *Biol Rev Camb Philos Soc* **82**, 591–605
549 (2007).

- 550 56. Jones, L. A. *et al.* Dynein light intermediate chains maintain spindle bipolarity by
551 functioning in centriole cohesion. *J. Cell Biol.* **207**, 499–516 (2014).
552 57. Klymkowsky, M. W. & Hanken, J. Whole-Mount Staining of *Xenopus* and Other
553 Vertebrates. *Methods in Cell Biology* **36**, 419–& (1991).
554

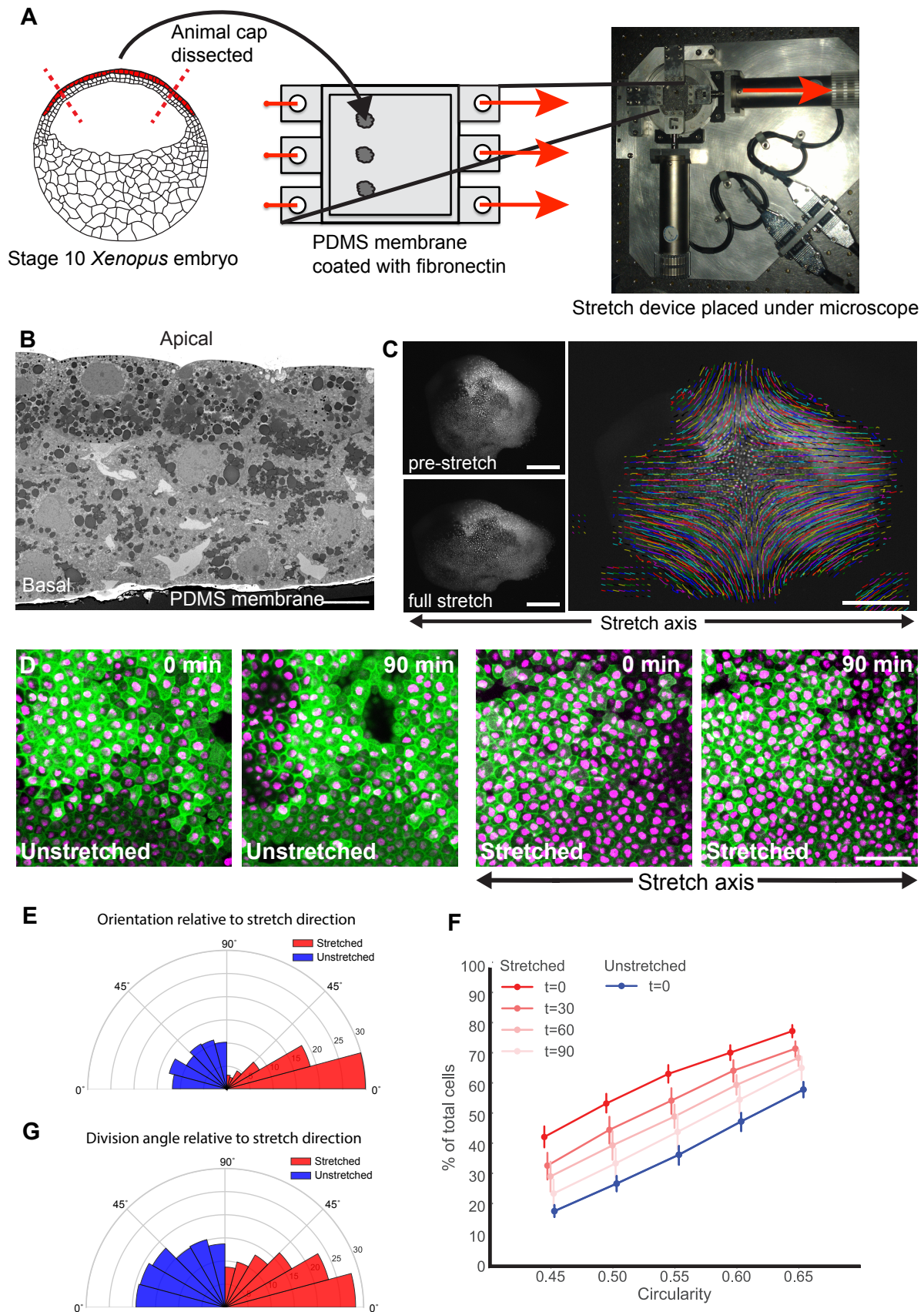


Figure 1: Application of tensile force to a multi-layered tissue. **A.** Animal cap tissue was dissected from Stage 10 *Xenopus laevis* embryos and adhered to fibronectin-coated PDMS membranes and a 35% uniaxial stretch of the membrane was applied. **B.** The animal cap tissue is 2-3 cells thick; cell shape and divisions were assessed in the apical cell layer. **C.** Displacement of nuclei in a stretched animal cap. **D.** Confocal images of the apical cells in unstretched and stretched animal caps (green: GFP-alpha-tubulin; magenta: cherry-histone2B), taken 0 and 90 minutes after stretch. **E.** Rose plot showing orientation of cell shape relative to direction of stretch in unstretched (blue) and stretched (red; measured immediately following stretch) experiments. **F.** Cumulative plots of cell circularity in unstretched (blue) and stretched (red; at 0, 30, 60 and 90 mins after stretch) animal caps (0=straight line; 1=circle). 100% of cells have circularity ≤ 1 . Markers slightly off-set for clarity. **G.** Rose plot of division angle relative to direction of stretch for unstretched (red) and stretched (blue) experiments. Kolmogorov-Smirnov test indicates that the unstretched distribution is not significantly different from a uniform distribution, $n = 343$ divisions, 15 animal caps; Kolmogorov-Smirnov test indicates that stretched distribution is significantly different from uniform, $p < 1.4 \times 10^{-9}$, $n = 552$ divisions, 17 animal caps. Scale bar: 10 μ m in **B**, 500 μ m in **C**, 50 μ m in **D**.

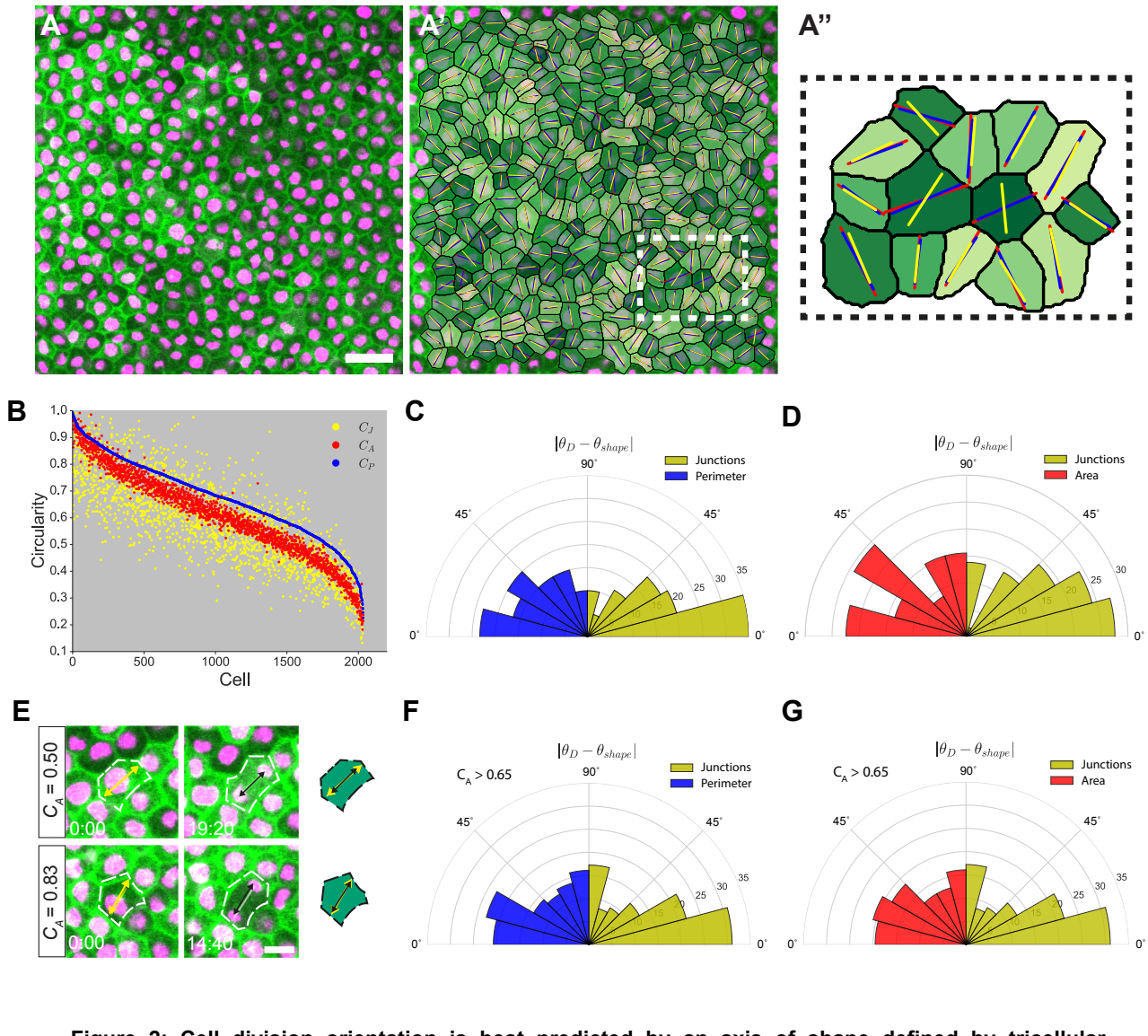


Figure 2: Cell division orientation is best predicted by an axis of shape defined by tricellular junctions. **A.** Representative image of control cells from an unstretched experiment. Scale bar: 20 μ m. **A'.** Overlay of segmentation of cells given in **A**, with the principal axis of shape characterised by area, perimeter and junctions drawn in red, blue and yellow respectively. **A''.** Enlargement of segmented cells from white box drawn in **A'**. **B.** Circularities of 2035 cells from unstretched experiments, with shape characterised by area, perimeter and junctions plotted in red, blue and yellow respectively. Cells have been ordered in descending order of perimeter-based circularity (C_P), with the corresponding values of C_A and C_J plotted alongside. **C.** Rose plot of difference between division angle, θ_D , and orientation of shape based on perimeter (blue; $\theta_{shape} = \theta_P$) and junctions (yellow; $\theta_{shape} = \theta_J$), for cells which satisfy $|\theta_P - \theta_J| \geq 15^\circ$. **D.** Rose plot of difference between division angle, θ_D , and orientation of shape based on area (red; $\theta_{shape} = \theta_A$) and junctions (yellow; $\theta_{shape} = \theta_J$), for cells which satisfy $|\theta_A - \theta_J| \geq 15^\circ$. **E.** Examples of round (top) and elongated (bottom) cells where division angle (black arrows) is well predicted by the principal axis of shape defined by area (yellow arrows). **F.** Rose plot of difference between division angle, θ_D , and orientation of shape based on perimeter (blue; $\theta_{shape} = \theta_P$) and junctions (yellow; $\theta_{shape} = \theta_J$), for round cells which satisfy $C_A > 0.65$. **G.** Rose plot of difference between division angle, θ_D , and orientation of shape based on area (red; $\theta_{shape} = \theta_A$) and junctions (yellow; $\theta_{shape} = \theta_J$), for round cells which satisfy $C_A > 0.65$.

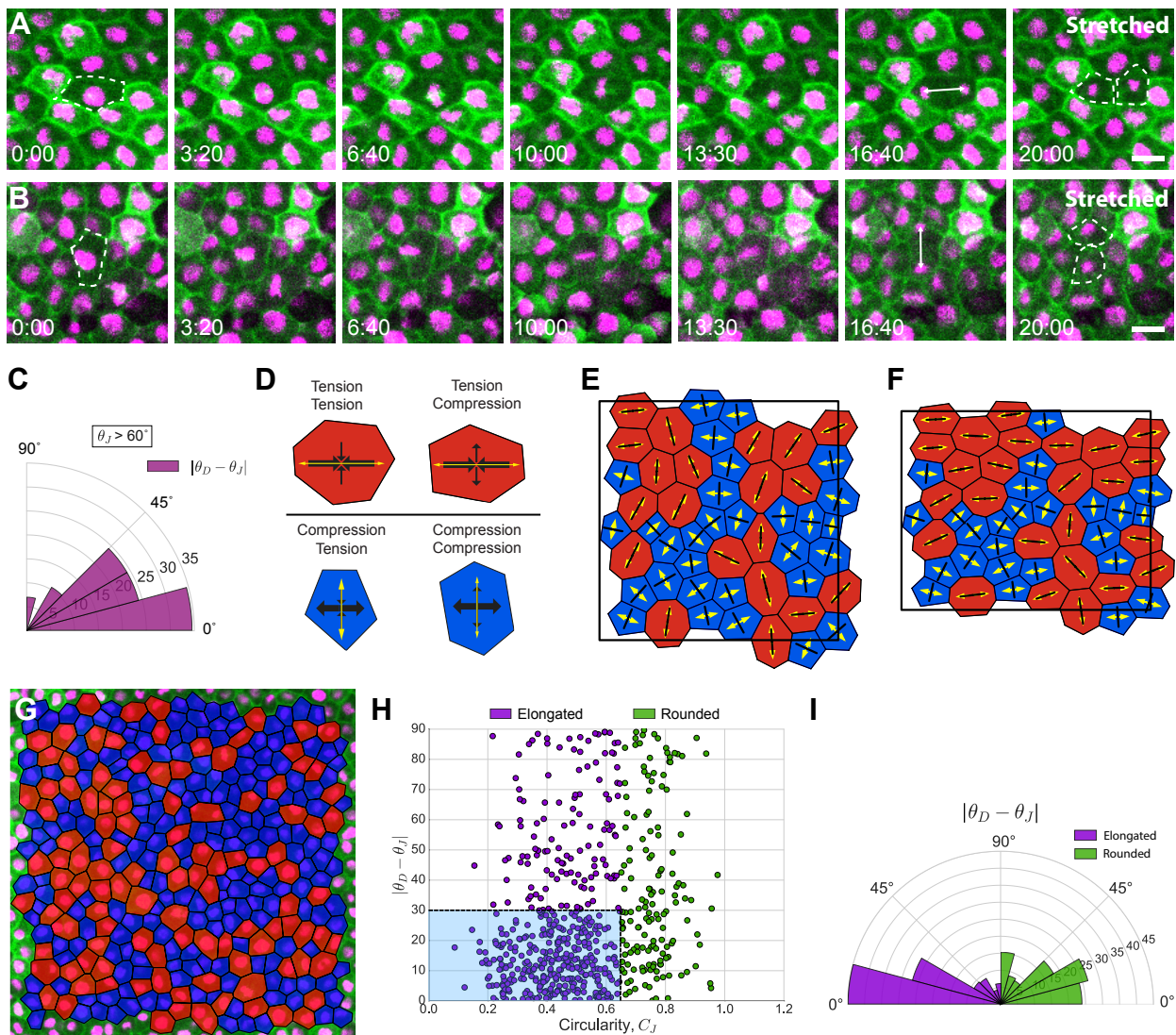


Figure 3: Local stress aligns with shape. Division orientation is better predicted by shape in elongated cells, rather than those with higher relative isotropic or shear stress. **A.** Images taken from a confocal timelapse movie of a division in a cell in stretched tissue whose interphase shape (dashed line, 0:00) is oriented with the stretch (horizontal) axis. Cell division aligns with both cell shape and stretch axis. **B.** Timelapse images of an unusual cell in a stretched tissue, whose interphase shape (dashed line, 0:00) is oriented against the stretch axis. Cell division aligns with cell shape but against the stretch axis. **C.** Rose plot of difference between division angle, θ_D , and orientation of shape based on junctions, θ_J , for cells from stretched experiments, where θ_J was at least 60° divergent to the direction of stretch. 29 cells satisfied this condition. Kolmogorov-Smirnov test found a significant difference from a uniform distribution ($p=0.022$). **D.** Representative cells showing classification of cell stress configurations. Red (blue) cells are under net tension (compression), where P^{eff} is positive (negative). Larger (smaller) black arrows indicate the orientation of the principal (secondary) axis of stress, with inward- (outward)-pointing arrows indicating the tension (compression) generated by the cell. Yellow arrows indicate the principal axis of shape defined by cell junctions, which aligns exactly with a principal axis of stress. **E.** 50 simulated cells randomly generated in a periodic box, relaxed to equilibrium with parameters $(\Lambda, \Gamma) = (-0.259, 0.172)$, under conditions of zero global stress (Nestor-Bergmann et al., 2017). Red (blue) cells are under net tension (compression). Principal axis of stress (shape) indicated in black (yellow). **F.** Cells from **E** following a 13% area-preserving uniaxial stretch along the x-axis. **G.** Example segmented cells from an unstretched experiment. Cells in red (blue) are predicted to be under net tension (compression). **H.** Cell circularity defined by junctions, C_J , vs $|\theta_D - \theta_J|$. Spearman rank correlation coefficient found a significant correlation ($p < 3.04 \times 10^{-10}$). Elongated cells ($C_J \leq 0.65$) cluster in blue box, whereas rounded cells ($C_J > 0.65$) have a more uniform distribution. **I.** Rose plot of difference between division angle, θ_D , and orientation of shape based on junctions, θ_J for round ($C_J > 0.65$; right) and elongated ($C_J \leq 0.65$; left) cells shown in **H**. Mann-Whitney U test indicated that elongated cells have θ_J aligned significantly more with θ_D than rounded cells ($p < 1.64 \times 10^{-8}$). Scale bar in **A&B**: 20 μ m. All rose plots show percentage of cells.

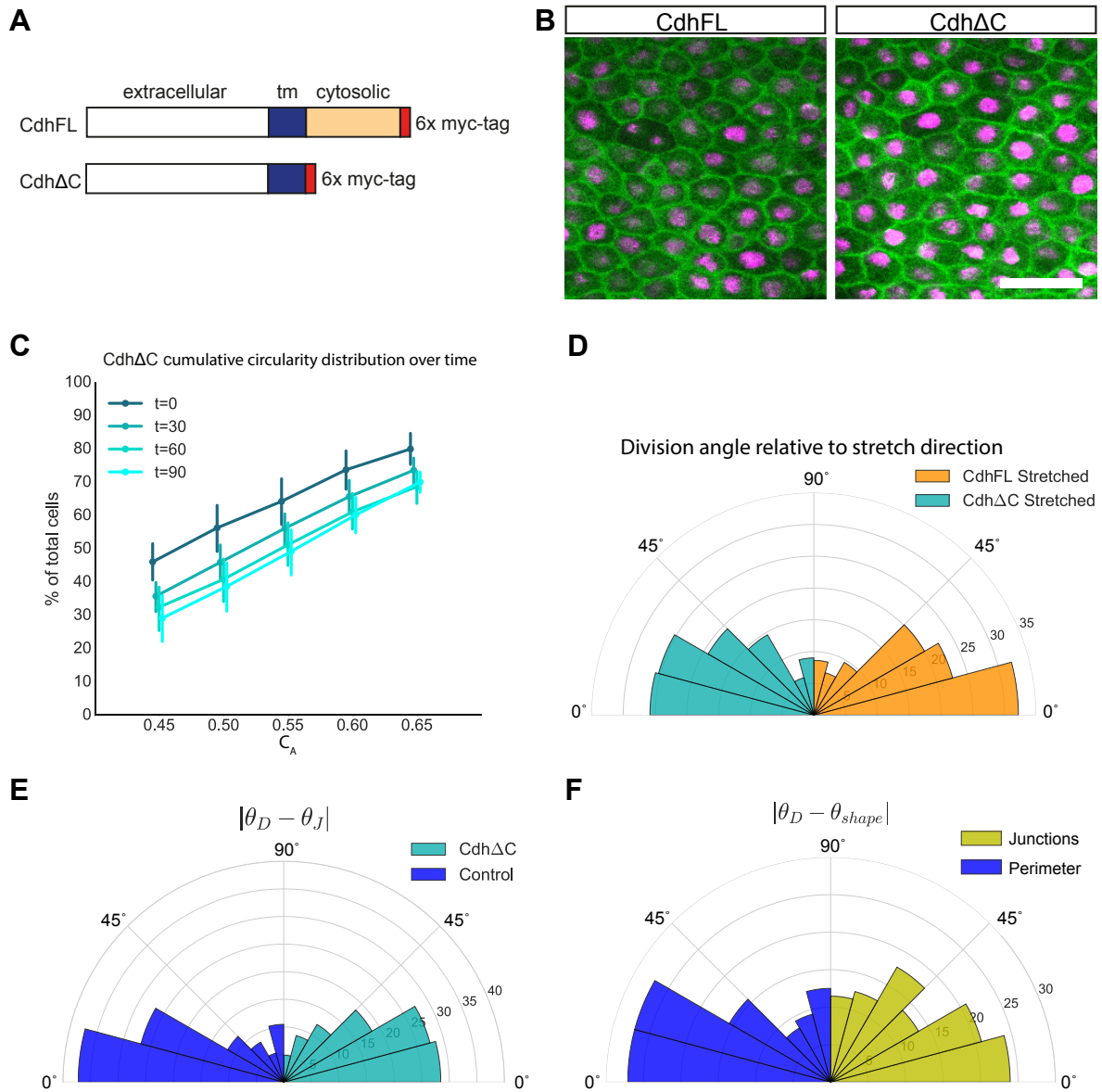


Figure 4: C-Cadherin is involved in orienting the mitotic spindle according to cell shape. **A.** Schematic of Cadherin constructs CdhFL and CdhΔC **B.** Images taken from a confocal timelapse movie of CdhFL- (left) and CdhΔC- (right) injected stretched animal cap explants. Scale bar 50μm. **C.** Cumulative plots of cell circularity defined by area, C_A , in CdhΔC-injected stretched animal caps at 0, 30, 60 and 90 mins after stretch (stretch applied just before 0 min). 100% of cells have $C_A < 1$. **D.** Rose plot of division angles, θ_D , relative to direction of stretch for cells from stretched CdhΔC-injected (411 cells; cyan) and stretched CdhFL-injected experiments (552 cells; orange). CdhFL-injected cells align significantly better with direction of stretch ($p < 0.0162$, Mann-Whitney U test). **E.** Rose plot of difference between division angle, θ_D , and orientation of shape based on junctions, θ_J , for cells from CdhΔC-injected experiments (390 cells; cyan) and control experiments (239 cells; blue). Distributions are significantly different ($p < 0.016$ Kolmogorov-Smirnov test). **F.** Rose plot of difference between division angle, θ_D , and orientation of shape based on perimeter, θ_p , (blue) and junctions, θ_j , (yellow) for 96 cells from CdhFL-injected experiments which satisfied $|\theta_p - \theta_j| \geq 15^\circ$. θ_D aligns significantly better to θ_p than a random distribution ($p < 0.004$; Kolmogorov-Smirnov test), but not to θ_j . Rose plots show percentage of cells.

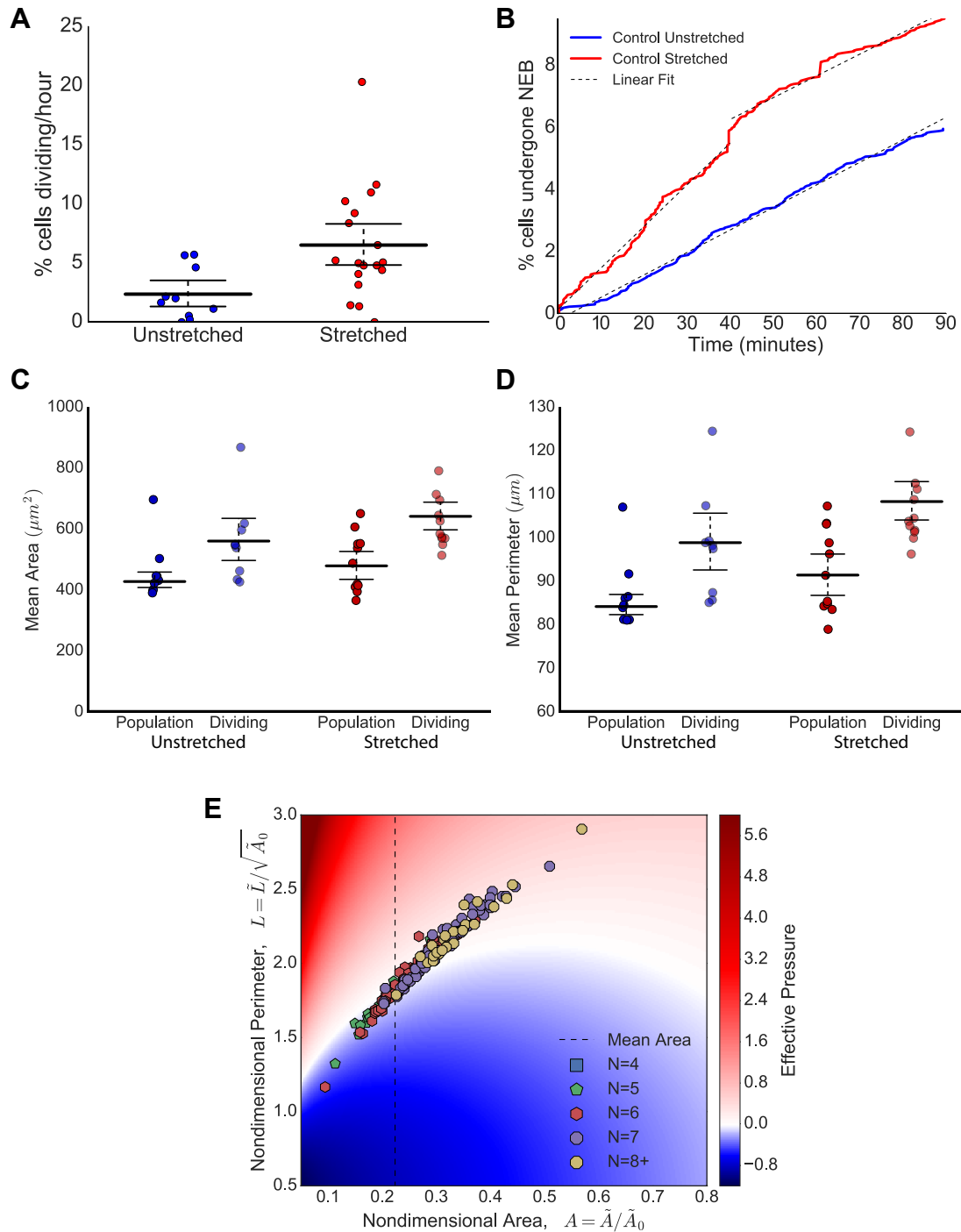


Figure 5: Stretching increases division rate. Dividing cells have large area, perimeter and relative effective pressure. **A.** Division rate (percentage of cells entering mitosis per hour) increases in stretched tissue compared to unstretched. 95% confidence intervals do not overlap, indicating significant difference. Each point represents the mean division rate from an animal cap. **B.** Percentage of cells that have undergone nuclear envelope breakdown (NEB) with respect to time in control stretched (red) and unstretched (blue) experiments from **A**. Dashed lines indicate linear lines of best fit; control unstretched experiments have gradient 4.2% cells undergoing division per hour. Stretched experiments have initial gradient 8.1% and then 4.35% cells undergoing division per hour. **C.** Comparison of mean area of population of all cells vs dividing cells from unstretched and stretched control experiments. Error bars represent mean and 95% confidence intervals, which do not overlap between the population and dividing cells, indicating a significant difference. **D.** Comparison of mean perimeter of population of all cells vs dividing cells from unstretched and stretched control experiments. Error bars represent mean and 95% confidence intervals, which do not overlap between the population and dividing cells, indicating a significant difference. **E.** Heat map showing predicted relative isotropic stress (effective pressure, P^{eff}) of dividing cells from control unstretched experiments. Areas and perimeters have been nondimensionalised using the preferred areas, \tilde{A}_0 , fitted to each experiment in Supplemental Figure 4C. Polygonal class (number of neighbours) indicated by marker colour and style, with (4,5,6,7,8+) sided cells given in (blue, green, red, purple, yellow). Dashed vertical line represents mean area of all cells. Cells lying in red (blue) regions are under predicted net tension (compression).

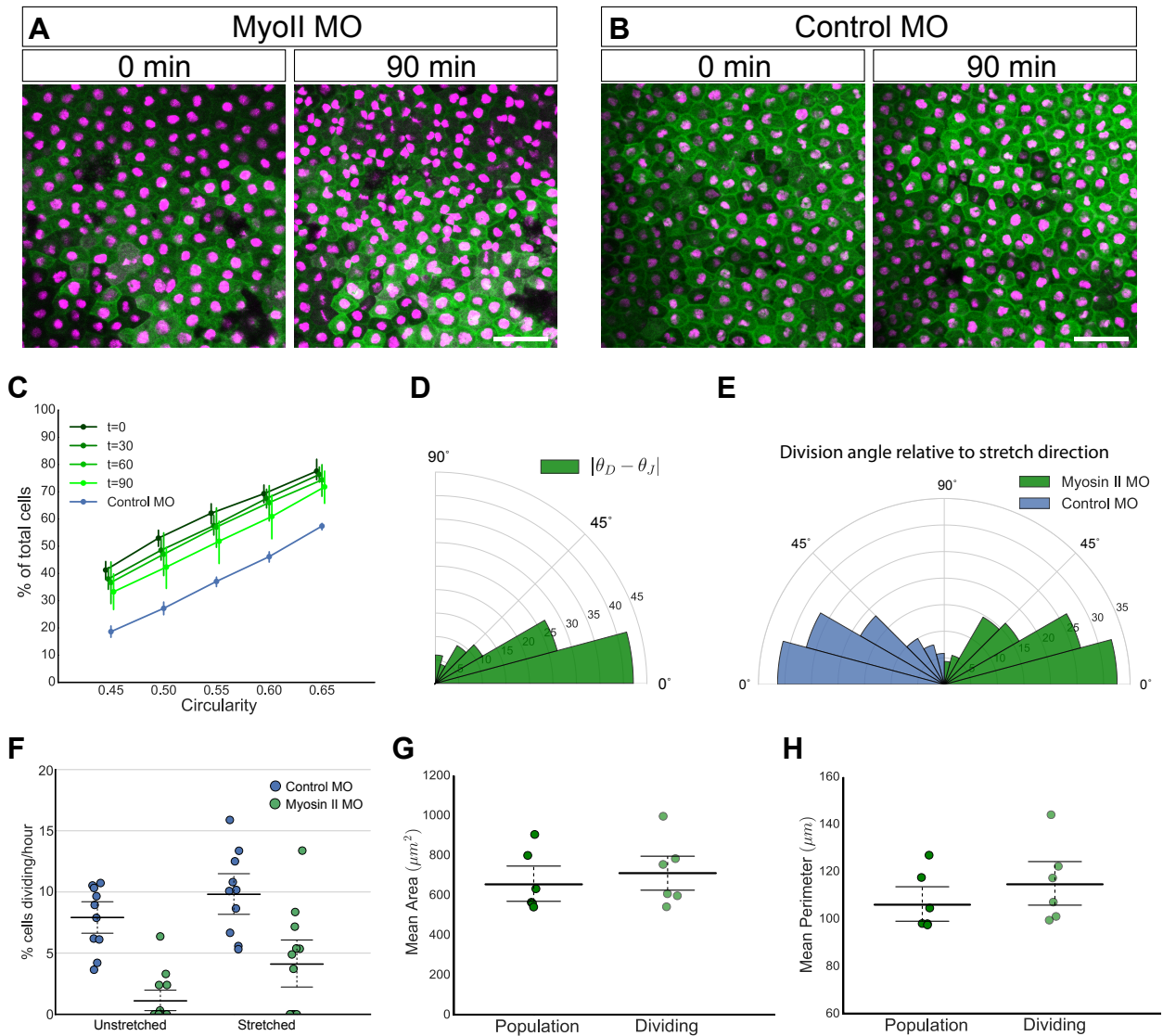


Figure 6: Myosin II MO cells maintain alignment of division to tricellular junctional shape, but have perturbed proliferation rate. **A.** Images taken from a confocal timelapse movie of stretched myosin II morpholino injected animal cap explants at 0 and 90 minute intervals. Butterfly nuclei seen prominently at 90 minutes, where nuclei are in contact. **B.** Timelapse images of control morpholino-injected stretched animal cap explants at 0 and 90 minute intervals. **C.** Cumulative distribution of cell circularity defined by area, C_A , in myosin II MO knockdown stretched animal caps (shaded green) at $t=0$, 30, 60 and 90 minutes after stretch. Cumulative distribution for unstretched $t=0$ control MO knockdown experiments shown in blue. Error bars represent 95% confidence intervals. Error bars for myosin II MO $t=90$ minutes distribution does not overlap with control MO, indicating a significant difference from unstretched shape. Markers are slightly off-set for clarity. **D.** Rose plot of difference between division angle, θ_D , and orientation of shape based on junctions, θ_J , for 216 cells from myosin II knockdown stretched experiments. Mann-Whitney U test found significant alignment compared to random ($p < 5.72 \times 10^{-15}$), but no significant difference from equivalent dataset in control stretched experiments. Percentages of cells shown. **E.** Rose plot of division angle relative to direction of stretch for control MO (532 cells; blue) and myosin II MO (301 cells; green) experiments. Mann-Whitney U and Kolmogorov Smirnov test found no significant difference between the two. **F.** Division rate (percentage of total cells entering mitosis per hour) in unstretched and stretched tissue from myosin II MO (green; $n=10$ for unstretched and $n=12$ for stretched) and control MO (blue; $n=13$ for unstretched and $n=10$ for stretched) experiments. Error bars represent mean and 95% confidence intervals. **G.** Comparison of mean area of population of all cells vs dividing cells from stretched myosin II knockdown experiments. Error bars represent mean and 95% confidence intervals, which overlap, indicating no significant difference. **H.** Comparison of mean perimeter of population of all cells vs dividing cells from stretched myosin II knockdown experiments. Error bars represent mean and 95% confidence intervals, which overlap, indicating no significant difference. Scale bar in **A** and **B**: $100\mu\text{m}$.

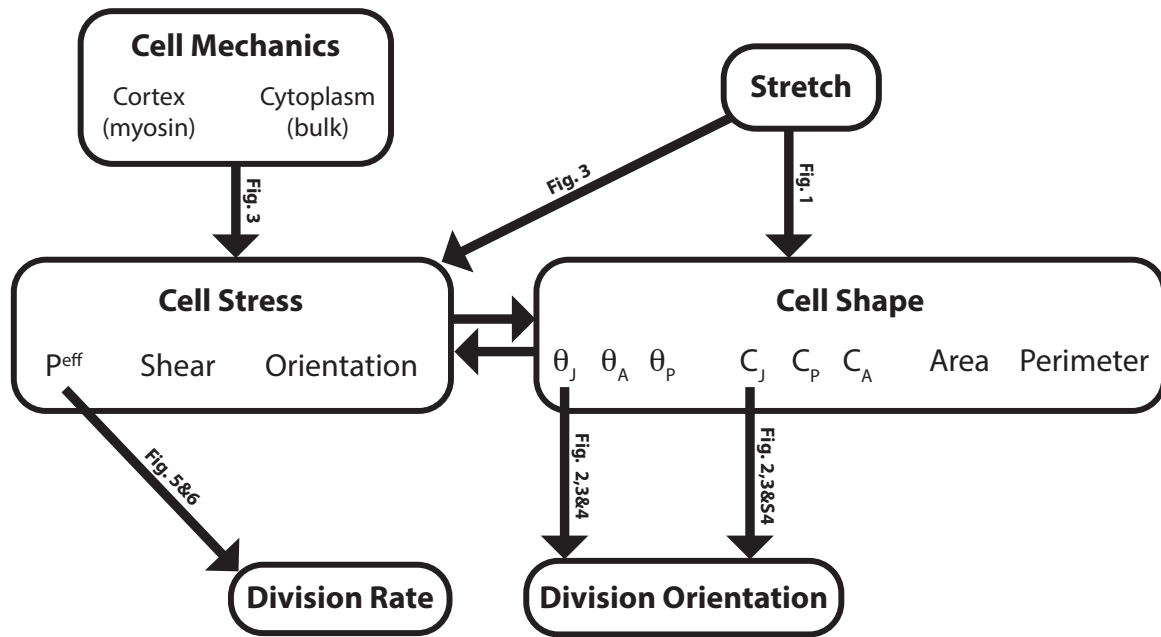


Figure 7: Putative network summarizing proposed division mechanisms. Rounded rectangles represent nodes of the network, with group names given in bold and sub-elements of the group written in regular font. Arrows represent lines of causality between nodes. Text along arrows reference Figures with data indicating that there is a causal link between two nodes or elements. Arrows connected to the boundary of a node indicate a causal link to/from all elements in the node. Arrows from sub-elements indicate the link is specifically only to/from the sub-element.